JOURNAL OF GEOPHYSICAL RESEARCH, VOL. 92, NO. B3, PAGES 2647–2661, MARCH 10, 1987

Variations in Oceanic Layer 2 Elastic Velocities Near Hawaii and Their Correlation to Lithospheric Flexure

THOMAS M. BROCHER

U.S. Geological Survey, Menlo Park, California

URI S. TEN BRINK

Lamont-Doherty Geological Observatory and the Department of Geological Sciences of Columbia University, Palisades, New York

Analysis of the travel times and amplitude range distributions of both compressional and shear wave arrivals on 15 closely spaced refraction profiles reveals a significant, systematic, and symmetric dependence of average layer 2 velocities on their distance to the north and south of the Hawaiian ridge. Beyond the flexural arch surrounding the ridge the velocity-depth solutions indicate a normal layer 2. Within the arch (approximately 155 km from the ridge) the average elastic velocities in layer 2 are lowered by 0.8–0.9 $\pm$ 0.2 km/s. Within 75 km of the ridge the average velocities are again normal. Elastic and elastic-plastic flexural models for the regional compensation of the Hawaiian islands predict tensional stress drops of 0.8 kbar in the upper lithosphere for the region having lowered velocities in layer 2, which are similar in magnitude with laboratory measurements of the confining pressure drop necessary to reduce velocities in porous basalts by 0.5 km/s. A significant inverse relationship (correlation coefficient of 0.818) exists between the average elastic velocities in the upper 1.0 km of the igneous crust and the strain in the upper crust calculated from these flexural models. The correlation between lowered average velocities in layer 2 and increased tensional stresses and strains suggest that crack opening in the upper crust accompanies the flexure. These observations are the first reported for a midplate load and corroborate previous suggestions from seismic and flexural data at subduction zones.

INTRODUCTION

It has long been known that the Hawaiian islands are associated with large-amplitude free-air gravity anomaly highs and lows that cannot be explained by models of local isotasy. These anomalies are flanked by a broad belt of low-amplitude positive anomalies. Because gravity anomalies are the surface expression of nonhydrostatic stresses at depth, these observations imply that significant deviatoric stresses exist, not only in the lithosphere under the islands but also farther away from the ridge. Flexural models that assume an elastic response by the lithosphere to vertical loading by the Hawaiian islands explain the regional gravity anomaly as well as other geological and geophysical observations [*Walcott*, 1970; *Watts and Cochran*, 1974]. The stresses predicted by these elastic models are high (> 1 kbar) and may exceed the failure strength of the upper lithosphere [*Brace and Kohlstedt*, 1980].

Seismic refraction and reflection data, Deep Sea Drilling Project (DSDP) cores, ophiolites, and laboratory-measured velocities of basalts suggest that oceanic crustal layer 2 comprises extrusive basalts that grade downward toward a sheeted dike complex [*Cann*, 1974; *Houtz and Ewing*, 1976; *Christensen*, 1978; *Spudich and Orcutt*, 1980; *Fox and Stroup*, 1981; *Anderson et al.*, 1982]. At DSDP site 504B where the crust is 6 m.y. old, *Anderson et al.* [1982] characterized the uppermost section of layer 2 (2A) as pillow basalts, breccias, and massive flows with freely connected fissures and pore spaces; the middle section of layer 2 (2B) is characterized by the same lithologies but has increased low-temperature precipitates in these voids; and the lowermost section of layer 2 (2C) is a transition zone between these basalts and breccias and the sheeted dike complex comprising the top of layer 3.

The inference made from DSDP drilling and logging results that seismic layer 2 comprises basaltic rocks of decreasing porosity is consistent with amplitude modeling of seismic refraction data from both the Pacific and Atlantic oceans [*Whitmarsh*, 1978; *Spudich and Orcutt*, 1980; *Bratt and Purdy*, 1984; G. M. Purdy, personal communication, 1985]. Thus the elastic velocities in layer 2 may depend primarily on the porosity of the basaltic rocks, and by inference from the effect of confining pressure on basaltic rock velocities [*Manghnani and Woollard*, 1968], on the state of tension or compression in layer 2.

Bodine et al. [1981] compared the calculated tensional strain in the upper crust of a subducting slab as a function of the distance from the outer trench high with velocity data obtained from sonobuoy measurements in the Izu-Bonin trench [*Houtz et al.*, 1980]. They found that a region of lowered velocities in layer 2 within 50 km of the bathymetric trench axis correlates with the region predicted to be in the highest tensional strain from a flexure model for the subducting slab. Sonobuoy refraction results from the Peru-Chile trench [*Hussong et al.*, 1975] also provide evidence for lowered layer 2 velocities within 50 km of the trench axis.

We present here a systematic study of layer 2 velocities near a midplate load. The Hawaiian ridge is a large midplate load on oceanic lithosphere of 80–90 m.y. age [*Atwater and Menard*, 1970]. Flexural models [e.g., *Bodine et al.*, 1981] predict that horizontal variations in the deviatoric stress will give rise to a laterally varying thickness to the brittle zone and to changes in the failure mechanism from compression near the island to tensional failure farther away (Figure 1).

During 1982 we obtained a suite of closely spaced high-quality digitally recorded refraction profiles near Oahu [*Watts et al.*, 1985] and these provide a data set to test for a systematic relationship between flexural strains and layer 2

Paper number 6B5979.
0148-0227/87/006B-5979$05.00

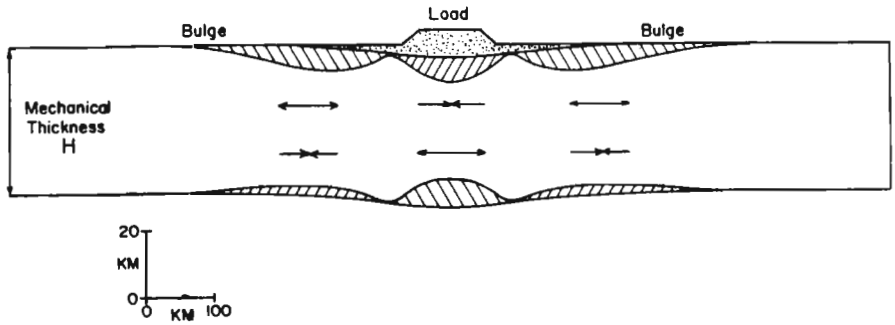

Fig. 1. Continuous deflection profile oriented NE-SW across the Hawaiian ridge produced using the yield stress envelope rheology showing the regions where the lithosphere is in compression and in tension. Load approximates the island of Oahu in the Hawaiian island chain on an 80-m.y.-old plate with assumed strain rate of 10^{-18} s^{-1}. Hatched regions indicate the extent of plastic yielding due to tensile (downslant to the right) and compressive (downslant to the left) bending stresses. H is the mechanical thickness [from *Bodine et al.*, 1981].

velocities. The existence of strong converted shear wave arrivals on these profiles permits a more rigorous, petrophysical interpretation of the velocity-depth solutions than is possible using compressional wave data alone. The gentle topography in this area facilitates comparison of the refraction profiles with each other and minimizes the influence of laterally variable crustal structure in their interpretation. Models of the lower crustal structure near Oahu inferred from the multichannel seismic reflection–refraction profiling are reported elsewhere (*Watts et al.* [1985]; U. S. ten Brink and T. M. Brocher, Multichannel seismic evidence for variations in crustal thickness across the Molokai fracture zone in the mid-Pacific, submitted to *Journal of Geophysical Research*, 1987) (hereafter referred to as tBB, 1987).

Data Acquisition

Nine expanding spread profiles (ESPs) and six fixed-gain sonobuoy profiles collected during the 1982 two-ship multichannel seismic experiment [*Watts et al.*, 1985] provide compressional and shear wave data in oceanic crust away from the Hawaiian islands. The 15 profiles are located between 73 and 300 km from the center of the Hawaiian ridge and were collected in water depths between 4360 and 4860 m (Table 1, Figure 2). Ten of the profiles are located on or close to the bathymetric arch, and 5 are located near the bathymetric moat surrounding the Hawaiian ridge; all were located on 80- to 90-m.y.-old oceanic crust [*Atwater and Menard*, 1970; *Ness et al.*, 1980; *Wallin*, 1982].

The acquisition and preliminary reduction of the ESP data is described elsewhere [*Watts et al.*, 1985; tBB, 1987]. The ESP data presented here were collected using a three-element airgun source array (totalling 31.66 L (1932 $inch^3$) and nominally operated at 124.1 bar (1800 psi) towed from the R/V *Kana Keoki*, received on a 3.6-km-long multichannel seismic streamer towed behind the R/V *Conrad*, and were recorded by a DFS-IV. The dominant bubble pulse frequency of this source is between 10 and 15 Hz. These multichannel data were sorted by range into 100 m wide bins; traces in each range bin (approximately 12) were summed after time shifting appropriate for a phase velocity of 8.0 km/s, and the summed traces were band-pass filtered between 6 and 20 Hz. Our choice of phase velocity used for time shifting the data means that the amplitudes of lower phase velocity arrivals are somewhat in error. These errors, however, are small because the bin is only 100 m wide: a 4-km/s arrival is undercorrected by a maximum of only 6 ms or 1/16th of a wavelength. Record sections were plotted in true relative amplitude. No corrections were applied for either topographic or sediment thickness variation.

Refraction data were also obtained using the identical airgun source array as used to collect the ESPs but instead shot to fixed-gain expendable military sonobuoy receivers deployed from the R/V *Kana Keoki*. Shot spacing was 120 to 150 m. Shot-to-receiver ranges for the sonobuoys were calculated from direct water wave arrival times assuming a speed of 1.50 km/s through the surface water. The relative shot-to-receiver ranges are considered to be accurate to within 20 m ($\pm$10 ms); at 25 km range uncertainties in absolute range may approach 200 m (for an uncertainty of the water velocity of $\pm$0.02 km/s). The sonobuoy data were digitally recorded, band-pass filtered between 6 and 20 Hz, and plotted in true relative amplitude. The sonobuoy data were uncorrected either for topographic variation or for lateral variations in the

TABLE 1. Division of ESP and Sonobuoy Profiles

Refraction Line No.	Distance From the Center of Load, km	Mean Water Depth, m	Observed Sediment Thickness TWTT, s	Calculated Sediment Thickness TWTT,* s
		Group 1		
SB 7	230	4475	0.27–0.42	0.35
SB 10	243	4395	0.25–0.30	0.27
SB 9	263	4450	0.22–0.30	0.26
ESP 1	263	4500	0.26–0.30	0.28
ESP 6	299	4395	0.13–0.20	0.16
		Group 2		
SB 6	180	4390	0.15–0.38	0.26
ESP 7	180	4450	0.25–0.30	0.27
		Group 3		
SB 4	154	4380	0.41–0.48	0.44
ESP 2	154	4370	0.40–0.50	0.45
SB 13	159	4360	0.25–0.30	0.27
		Group 4		
ESP 8	117	4725	0.55–0.62	0.59
ESP 3	130	4445	0.45–0.50	0.49
		Group 5		
ESP 9	73	4860	1.15–1.20	1.17
ESP 4	74	4700	0.98–1.08	1.03
ESP 11	75	4730	1.15–1.32†	1.22

*Calculated from the velocity-depth models given in Table 2.
†The CDP line for ESP 11 is not coincident with the ESP profile.

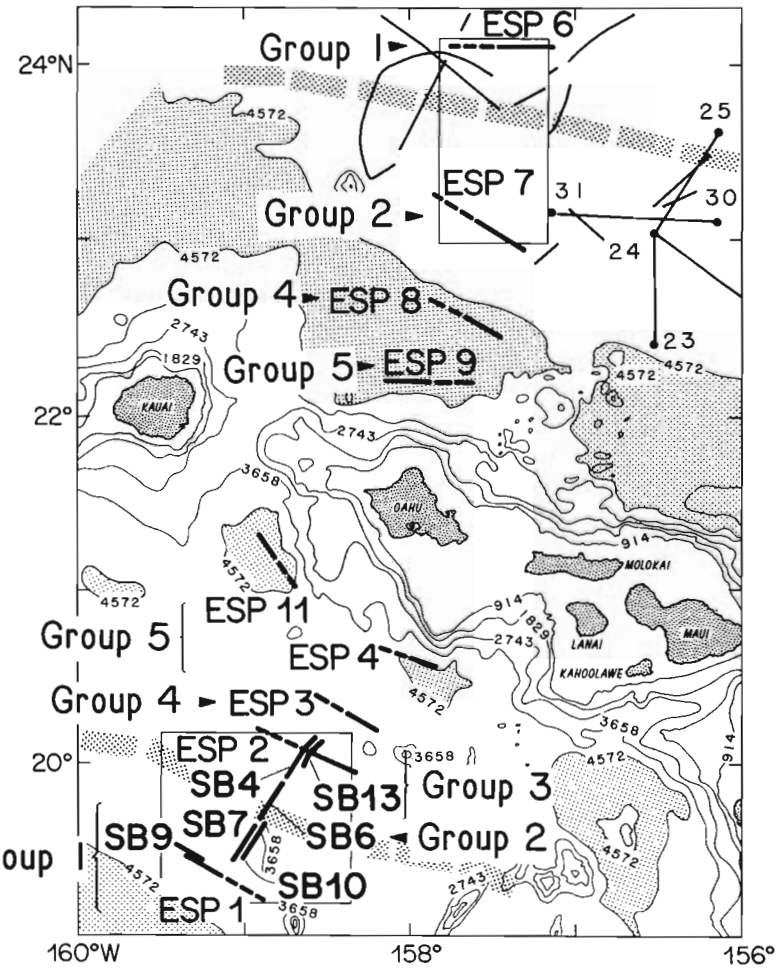

Fig. 2. Location of ESPs (numbered bold-dashed and solid lines) and sonobuoy refraction profiles (labeled SB) interpreted for this study. Boxed areas indicate locations of expended bathymetric maps shown in Figure 5. Locations of profile groupings 1–5 are indicated by brackets and arrows. Numbered straight line segments (numbers 26–30) correspond to refraction lines collected by *Shor and Pollard* [1964]; thinner unlabeled arcuate and straight line segments near ESP's 6 and 7 show shot points of data collected by Shor and Pollard and *Morris et al.* [1969]. Location of the arch surrounding the Hawaiian ridge is indicated by bold stippled dashed lines whereas depths greater than 4572 m (including the moat surrounding the ridge) are lightly stippled. Bathymetry given in 914.4 m (500 fathom) contour intervals.

sediment thickness. Because the sonobuoy data consist of single source and receiver pairs, lateral variations produce more noticeable effect than for the ESPs.

Refraction Data: Prominent Features

We have subdivided the refraction profiles into five groups numbered 1 through 5 solely in order of decreasing distance from the center of the Hawaiian ridge. This division, however, highlights the similarity between seismic profiles in similar geographic locations and differences between groups of profiles.

Group 1

The first group consists of 5 profiles collected at a distance of 230 to 300 km from the center of the Hawaiian ridge (Table 1, Figure 2). These profiles are characterized by a single strongly curved crustal compressional-wave refraction that can be recognized to distances of at least 16 km (Figure 3) and large-amplitude converted shear-wave arrivals (Figure 4).

Group 2

The second group of refraction profiles consists of two profiles located about 180 km from the Hawaiian ridge (Table 1, Figures 2 and 5). This group of profiles is characterized by two different compressional-wave refractors and by weak converted shear-wave arrivals at ranges less than 25 km (Figures 6 and 4). Low amplitudes and low velocities (3.7–4.3 km/s) characterize the first refraction. The second refractor emerges from the seafloor reflection with a phase velocity between 4.5 and 5.3 km/s and becomes strongly focused at ranges between 9 and 15 km.

Group 3

This group consists of 3 refraction profiles collected at ranges about 154 to 159 km from the Hawaiian ridge (Table 1, Figure 2). The compressional-wave arrivals in this group, such as ESP 2 (Figure 6), are characterized by two discrete refractions with phase velocities of between 3.7 and 3.9 km/s and 5.8 to 6.5 km/s. The faster refraction is strongly focused at ranges between 7 and 10 km (Figure 6). The converted shear wave arrivals for group 3 profiles are generally difficult to identify (Figure 4). The travel times of both compressional and shear waves of layer 3 arrivals (having phase velocities of 6.5 or 3.5 km/s) for this group are significantly delayed relative to those of the groups 1 and 2 refraction profiles (Figure 9).

Group 4

The fourth group consists of two profiles collected at ranges between 117 and 130 km from the Hawaiian ridge (Table 1,

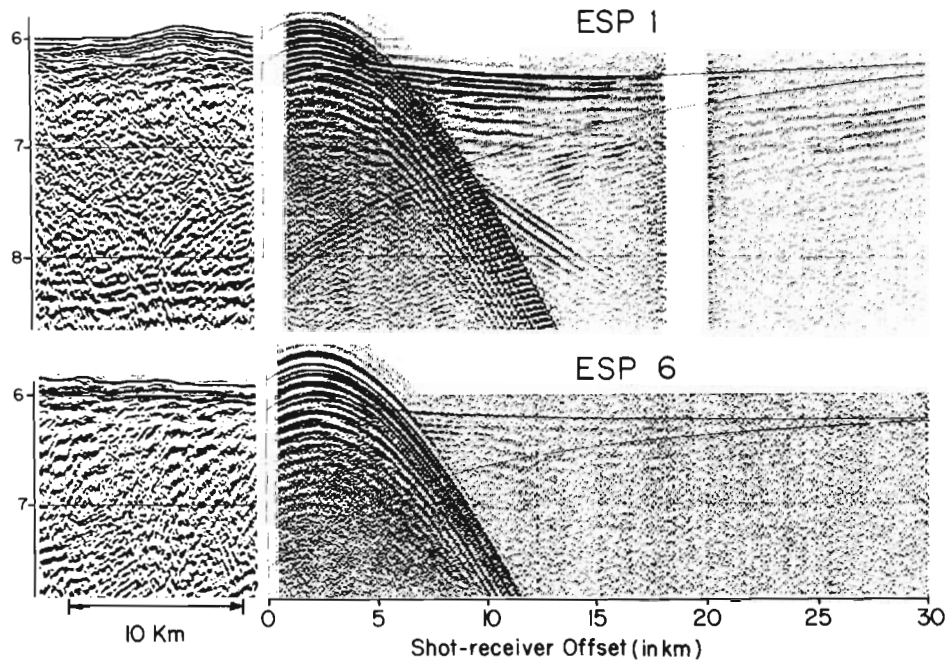

Fig. 3. Comparison of the reduced (at 6.5 km/s) record sections for two ESPs in group 1 showing the crustal first arriving compressional waves. Thin solid curves show travel times calculated from the inferred velocity-depth solutions in Table 2. Shown to the left of each ESP is the CDP section which was collected along the refraction profile at the ESP midpoint. Time scales are the same for the CDP and ESP profiles.

Figure 2). Although the compressional wave first arrivals of both profiles in this group are characterized by a large amplitude, 4.2-km/s refraction, there is little resemblance between the later refraction branches on these profiles (Figure 7). On ESP 3 the first refractor is strongly curved and leads continuously into secondary refraction branches having phase velocities of 5.5 and 6.7 km/s. These secondary branches show strong focusing of energy at ranges between 13 and 22.5 km. On ESP 8 the 6.7 km/s refractor is focused at ranges between 8 and 11 km.

Group 5

The last group consists of 3 refraction profiles collected at ranges of about 74 km from the ridge (Table 1, Figure 2). Figure 8 shows that these profiles were all collected in the bathymetric moats flanking Oahu in water depths exceeding 4600 m. The profiles in this group resemble each other only in having two distinct sets of compressional arrivals and weak shear arrivals (Figure 7). The first refraction has phase velocities between 4.0 and 4.2 km/s. On ESPs 4 and 11 the second refraction, having a phase velocity close to 6.5 km/s, is focused at ranges between 10 and 18 km. On ESP 9 the secondary refraction arrivals are strongly focused at 12 km range (Figure 7).

DATA INTERPRETATION

Inversion of the densely sampled seismic refraction profiles via tau sum analysis of slant stacks of the records [*Diebold and Stoffa*, 1981] provided initial estimates of velocity-depth solutions. In most cases, forward modeling of the travel times using velocity-depth functions inferred in this manner did not provide a close fit to the observations. We attribute the lack of success of the tau sum inversion technique to the relatively low signal-to-noise ratio of the profiles and slant stacks. For these data we therefore preferred to employ the more subjective interpretation method of iterative forward modeling of travel times assuming one-dimensional structure. For all models the amplitude range distribution was qualitatively analyzed by plotting the calculated ray density along the travel time branches. Because this method does not easily yield formal uncertainties in either layer thicknesses or velocities, in the rest of this section we review, layer by layer, the constraints upon and uncertainties inherent in the solutions.

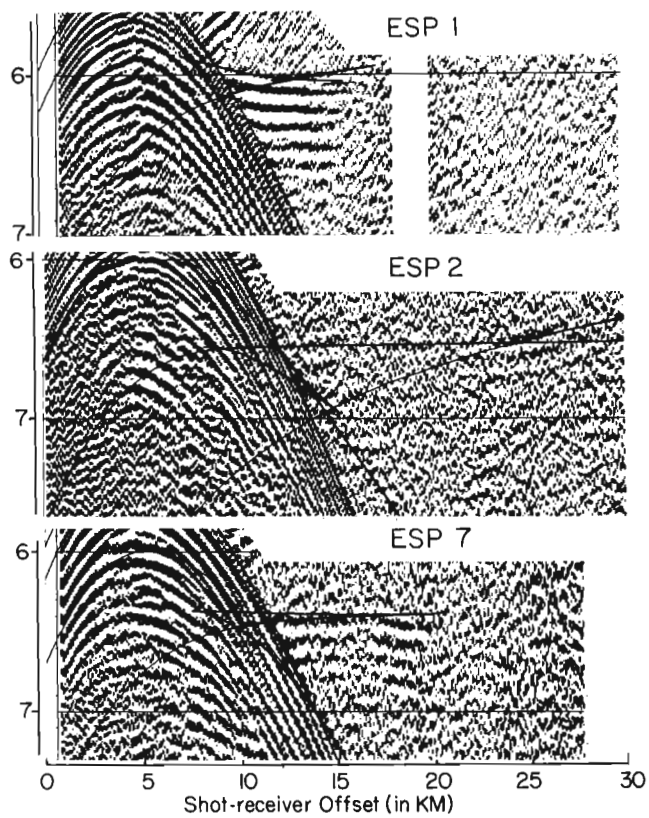

Fig. 4. Comparison of the reduced (at 3.5 km/s) record sections for three refraction profiles showing the crustal first arriving shear wave arrivals. Thin solid curves show the travel times calculated from the inferred velocity-depth solutions in Table 2.

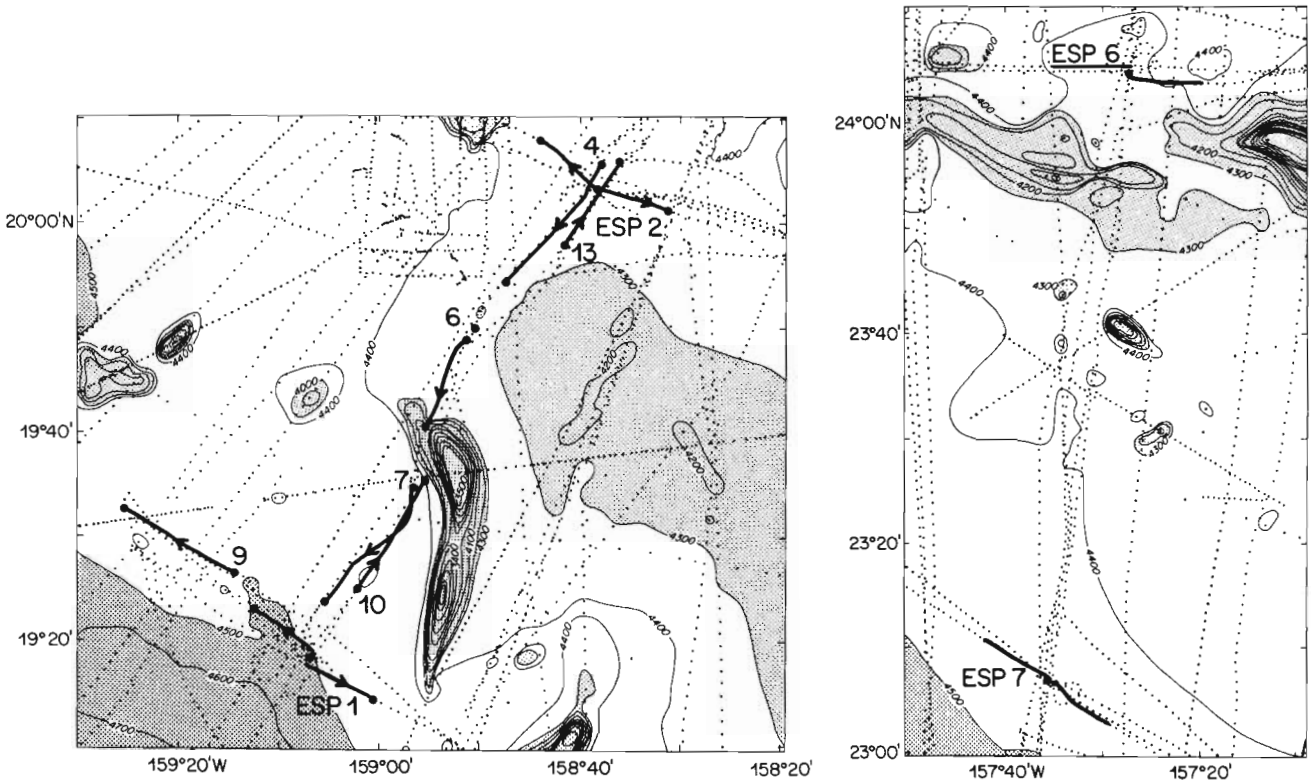

Fig. 5. Detailed bathymetry maps show the locations of the ESPs and sonobuoy refraction profiles for groups 1–3. Large solid dots at the center of the ESPs indicate ESP midpoints. Arrows on sonobuoy profiles indicate direction ship travelled after deploying the sonobuoy. Bathymetry, contoured in 100 m intervals, is based on single-beam 3.5-kHz soundings along the ship tracks shown as dotted curves. Depths exceeding 4500 m and less than 4300 m are shaded.

Sediments

The refraction data do not provide constraints on either the thickness or velocity of the uppermost pelagic sediments. Nearby DSDP results at site 67 suggest that velocities of 1.5 and 1.7 km/s are appropriate for these sediments [*Winterer et al.*, 1971]; this velocity range was assumed in our models. Reflection profiles collected during our experiment and in previous experiments [*Kroenke*, 1965; *Normark and Shor*, 1968; *Von Herzen et al.*, 1982; *Wallin*, 1982] suggest the presence of a 120- to 350-ms thickness (two-way travel time (TWTT)) of pelagic sediments. The thicknesses of pelagic sediments used in the modeling are thus inferred from the assumed velocity and measured TWTT. Uncertainties in the observed TWTT of 25–50 ms correspond to uncertainties in the thickness of this pelagic layer of 22–43 m.

For groups 2 through 5 an additional layer of higher velocity sediments is required by the refraction data. As this sedi-

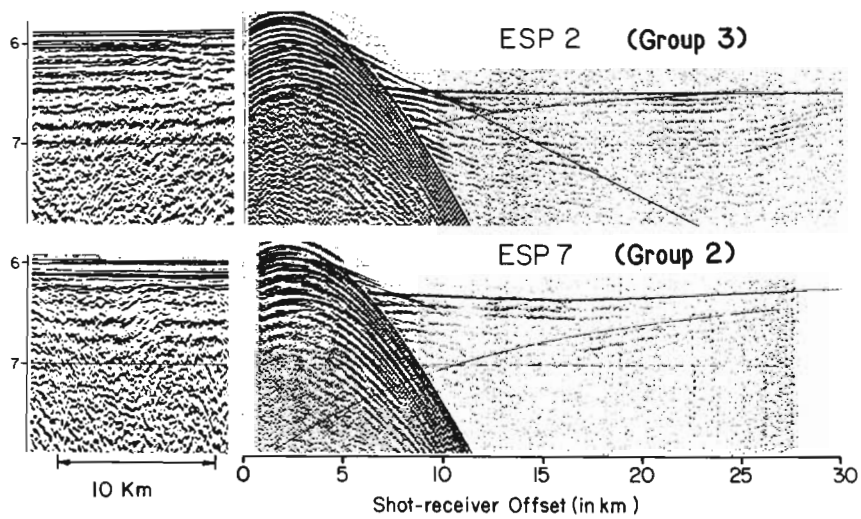

Fig. 6. Comparison of the reduced (at 6.5 km/s) record sections for all the ESP profiles in groups 2 and 3 showing the crustal first arriving compressional waves. Thin solid curves show travel times calculated from the inferred velocity-depth solutions in Table 2. Shown to the left of each ESP or sonobuoy profile is the CDP section which was collected along the refraction profile at the midpoint of the ESP. Time scales are the same for the CDP and ESP profiles.

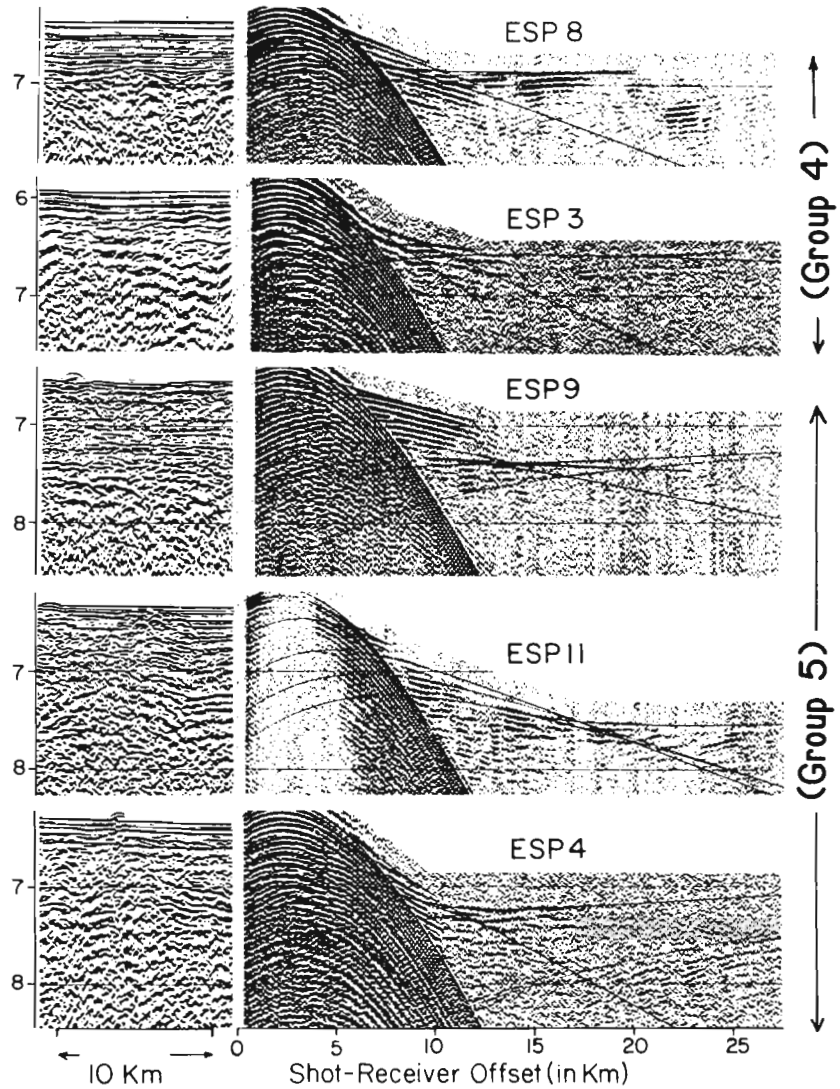

Fig. 7. Comparison of the reduced (at 6.5 km/s) record sections for all the refraction profiles in groups 4 and 5 showing the crustal first arriving compressional waves. To the left of each ESP is shown the CDP section which was collected along the refraction profile. Time scales are the same for the CDP and ESP profiles.

ment layer produces first arrivals with phase velocities between 3.7 and 4.4 km/s, its velocity and thickness can be uniquely determined from the phase velocity, intercept time, as well as the TWTT on the coincident common depth point (CDP) reflection profiles. On CDP records the top of the igneous basement can be identified as the first topographically irregular low-frequency reflection below more planar and higher frequency reflections inferred to be sediments. Average uncertainties in the TWTT of this second sediment layer of 90 ms translate into average uncertainties in layer thickness of approximately 0.2 km. A comparison between the observed TWTT through the sediments and those calculated from the velocity models in Table 2 is provided in Table 1.

Layer 2A

No direct estimate of the velocities within layer 2A is available. Indirect evidence for these velocities derives from three principal sources. First, the presence on group 1 profiles of large-amplitude converted shear wave arrivals having phase velocities of 3.5 km/s suggests that for these profiles the compressional-wave velocity at the top of layer 2A is significantly higher than 3.5 km/s [*Spudich and Orcutt*, 1980; *White and Stephen*, 1980]. Following *Spudich and Orcutt* [1980] we assumed a compressional wave velocity of 4.2 km/s for these profiles and that the conversion to shear wave energy from the incident *P* wave energy occurred at the unlithified sediment-igneous basement interface. Second, propagation of rays up and down through this layer introduces time delays in the intercept times for the 6.5 km/s arrivals which are observed. This constraint imposes limitations on the average velocity and thickness of the layer. Uncertainties in the intercept times are about 13 ms, whereas the uncertainty in the intercept time delay through layers 2A and 2B (the difference between two intercept times) is about 25 ms. Third, for some refraction profiles the presence of low-velocity gradients within layer 2A was inferred from the rapid amplitude decay with range of refractions having phase velocities comparable to the velocities used to model layer 2A.

Layer 2B

Arrivals refracted by layer 2B are observed on the refraction profiles and thus provide direct evidence for the velocity and thickness of this layer. Even if this constraint is ignored, layer 2B introduces an additional intercept time delay for the 6.5-

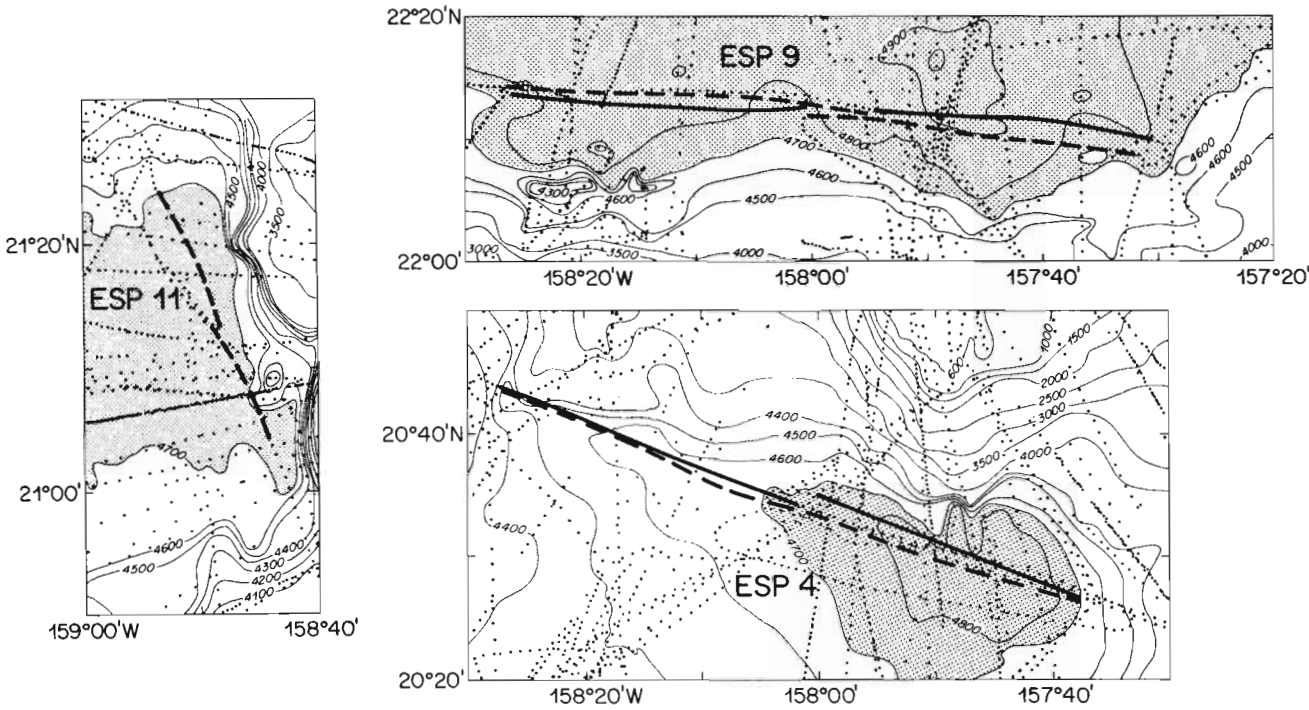

Fig. 8. Bathymetry in corrected meters near the ESP's of group 5 profiles. Contour interval changes from 500 m shallower than 4000 m depth to 100 m below, with depths below 4700 m shaded. Heavy dashed curves indicate the locations of the ships for the airgun portion of the ESP; the heavy solid curves indicate the ship tracks for the explosive portion of the ESPs (not used in this study). Small dots show locations of bathymetric data compiled in these maps.

km/s refraction, which places constraints on the average velocity and combined thickness of layers 2A and 2B. Further constraint on layer 2B is possible using triplications in the observed refraction arrivals between 7 and 12 km range, which require significant velocity gradients within layer 2B. This high velocity is similar to one used by *Bratt and Purdy* [1984] to explain strong amplitude peaks at ranges between 7 to 10 km range on ocean bottom seismometers for surface sources and receivers; these ranges correspond to 8–11 km for the water depths appropriate for groups 1–3.

Uncertainties in Average Velocities Through Layers 2A and 2B

In order to quantify the velocity models in Table 2, we have calculated in Table 3 average velocities in the upper 1 km of the igneous crust (corresponding to layers 2A and 2B). Treating layers 2A and 2B as a single 1-km-thick layer, the uncertainty in the average velocity of the layer can be estimated from the uncertainty in its intercept time delay using $\Delta t = |2hq_1 - 2hq_2|$, or

$$q_1 = q_2 \pm \Delta t/2h \tag{1}$$

where $q_{1,2} = ((v_{1,2})^{-2} - p^2)^{1/2}$; h is the layer thickness; $v_{1,2}$ are two average velocities through layers 2A and 2B; Δt is the uncertainty in intercept time delay; and p is the ray parameter of the observed refraction. In this estimate of the uncertainty the layer thickness is held fixed: it is also possible to attribute the uncertainty in Δt to relatively minor changes in layer thickness. As an example, using $h = 1$ km, $p = (6.5)^{-1}$ s/km, $\Delta t = 25$ ms, and $v_2 = 4.4$ km/s, we find that $v_1 = 4.7$ km/s. The uncertainties are thus ± 0.3 km/s for average velocities in layers 2A and 2B for group 3 (Table 3). In Table 3 we have compiled the uncertainties in average velocities using (1) for all profiles as well as the intercept time delay introduced by layers 2A and 2B for later arrivals having a phase velocity of 6.5 km/s. The table documents that the models predict that differences in the delay time introduced by these layers between groups 1 and 3 exceed measurement errors (Figure 9).

Layer 2C

Layer 2C produces first arrivals which decay rapidly in amplitude with range. For this reason the velocity gradient within this layer was generally modeled as being relatively low. For some profiles a higher-velocity gradient within layer 2C was necessary to explain triplication peaks at 12.5–23 km range.

RESULTS

Sediments

To explain the observed TWTT and intercept time delays in the sediments the velocity-depth solutions require up to 250 ± 43 m of pelagic sediments having an assumed velocity of 1.5–1.7 km/s (Figure 10). To fit the first arrival times of the groups 2 through 5 profiles, an additional layer of higher velocity sediments is required. This layer has velocities from 3.7 to 4.4 km/s and varied in thickness between 480 and 2670 ± 200 m (Figure 10). The velocities of this sedimentary wedge are appropriate for turbidite or volcanoclastic sequences derived from the Hawaiian ridge. In the following section presenting the solutions for layer 2, and the depths cited are those measured down from the top of the igneous crust.

Group 1

The compressional-wave velocity-depth solutions for the group 1 profiles characterize layer 2A as a zone of having a

TABLE 2. Velocity-Depth Solutions for Sonobuoy Profiles and ESPs

Layer Number	Layer Thickness, km	V_p, km/s (Top/Bottom)	Layer Thickness, km	V_s, km/s (Top/Bottom)	σ (Top/Bottom)
		Sonobuoy 7			
1	0.24	1.5/1.6	0.24		
1A	0.09	4.3/4.5			
2*	0.41	4.5/5.8	0.94	2.2/3.3	0.32/0.30
2A	0.60	5.8/6.2	...	...	...
3	0.65	6.2/6.9	0.50	3.3/3.6	0.30/0.31
4	0.60	6.9/7.1	0.60	3.6/3.9	0.31/0.28
5	5.00	7.1/7.3	3.00	3.9/4.1	0.28/0.27
		Sonobuoy 10			
1	0.21	1.5/1.6	0.23		
2	0.02	1.6/1.6	0.02		
3*	0.46	4.5/5.7	0.90	2.3/3.3	0.32/0.29
3A	0.70	5.7/6.1	...	...	...
4	0.40	6.1/6.4	0.50	3.3/3.5	0.29/0.28
5	0.50	6.4/6.7	0.50	3.5/3.7	0.28/0.28
6	5.40	6.7/7.3	4.00	3.7/4.1	0.28/0.27
		Sonobuoy 9			
1	0.17	1.5/1.6	0.15		
2	0.09	4.2/4.5			
3*	0.41	4.5/5.6	0.90	2.3/3.0	0.28/0.33
3A	0.40	5.6/6.0	...	...	...
4	1.35	6.0/6.7	1.40	3.5/3.7	0.25/0.28
5	3.40	6.7/7.1	3.40	3.7/3.9	0.28/0.28
		ESP 1			
1	0.20	1.5/1.6	0.16		
2	0.04	4.2/4.3			
3*	0.51	4.3/5.7	0.42	2.3/3.1	0.28/0.28
3A	0.40	5.7/6.0	0.72	3.1/3.4	0.28/0.27
4	1.90	6.0/6.9	0.24	3.4/3.5	0.28/0.29
4A	...	...	0.30	3.5/3.7	...
4B	...	...	0.28	3.7/3.8	0.29/0.26
5	3.00	6.9/7.2			

Sonobuoy 6			ESP 6		
Layer Number	Layer Thickness, km	V_p, km/s (Top/Bottom)	Layer Number	Layer Thickness, km	V_p, km/s (Top/Bottom)
1	0.09	1.7/1.7	1	0.12	1.5/1.5
2	0.14	4.0/4.2	2*	0.09	1.5/1.6
3	0.17	4.2/4.2	3	0.50	4.2/5.7
4*	0.31	4.2/4.2	4	0.47	5.7/6.2
5	0.60	4.5/5.1	5	0.40	6.2/6.3
6	0.20	5.1/6.1	6	0.40	6.3/6.4
7	0.80	6.1/6.4	7	2.20	6.4/6.7
8	1.05	6.4/6.9			
9	0.20	6.9/7.0			
10	3.00	7.0/7.0			

Layer Number	Layer Thickness, km	V_p, km/s (Top/Bottom)	V_s, km/s (Top/Bottom)	σ (Top/Bottom)
		ESP 7		
1	0.18	3.7/4.3	1.8/2.0	0.40/0.37
2	0.13	4.3/4.4	2.1/2.1	0.34/0.34
3	0.21	4.2/4.2	2.1/2.1	0.34/0.34
4*	0.21	4.2/4.2	2.1/2.1	0.34/0.34
5	0.53	4.5/5.1	2.1/2.7	0.30/0.30
6	0.20	5.1/6.1	2.7/3.5	0.30/0.26
7	0.80	6.1/6.4	3.5/3.6	0.26/0.28
8	1.05	6.4/6.9		
		ESP 2		
1	0.03	1.7/1.7		
2	0.14	3.85/3.9	2.0/2.2	0.31/0.28
3	0.66	3.9/3.9	2.2/2.2	0.28/0.28
4*	1.00	4.2/4.9	2.3/2.6	0.28/0.29
5	0.18	4.9/6.1	2.6/3.5	0.30/0.25
6	0.19	6.1/6.2	3.5/3.5	0.25/0.25
7	0.73	6.2/6.6	3.6/3.8	0.25/0.29
8	0.62	6.6/6.6		

Sonobuoy 4			Sonobuoy 13		
Layer Number	Layer Thickness, km	V_p, km/s (Top/Bottom)	Layer Number	Layer Thickness, km	V_p, km/s (Top/Bottom)
1	0.20	1.7/1.7	1	0.06	1.7/1.7
2	0.39	3.9/3.9	2	0.39	3.9/3.9
3*	0.20	3.9/3.9	3*	0.37	3.9/3.9
4	0.75	4.2/4.9	4	0.90	4.2/4.9
5	0.18	4.9/6.1	5	0.18	4.9/6.1
6	0.92	6.1/6.6	6	1.90	6.1/6.9
7	0.62	6.6/6.7			
8	1.08	6.7/7.0			

ESP 3			ESP 8		
Layer Number	Layer Thickness, km	V_p, km/s (Top/Bottom)	Layer Number	Layer Thickness, km	V_p, km/s (Top/Bottom)
1	0.03	3.4/3.4	1	0.04	1.7/1.7
2	0.95	4.0/4.0	2	0.49	4.2/4.4
3*	0.18	4.3/4.7	3	0.31	4.3/4.3
4	0.52	4.7/5.1	4	0.34	4.3/4.4
5	0.29	5.1/5.6	5*	0.38	4.4/4.4
6	0.37	5.6/5.9	6	0.17	4.9/5.7
7	1.09	6.2/6.2	7	0.58	5.9/6.4
8	0.82	6.3/6.8	8	0.71	6.4/6.6

ESP 9			ESP 4		
Layer Number	Layer Thickness, km	V_p, km/s (Top/Bottom)	Layer Number	Layer Thickness, km	V_p, km/s (Top/Bottom)
1	0.34	3.1/4.6	1	0.66	3.2/3.6
2	0.69	4.6/4.9	2	0.69	3.8/3.8
3	0.47	5.0/4.0	3	0.51	3.9/4.3
4	0.95	4.0/4.3	4	0.07	4.7/4.8
5	0.08	5.1/5.1	5*	1.00	4.8/6.0
6*	0.58	5.1/5.1	6	0.96	6.0/6.9
7	0.67	6.1/6.2	7	0.32	6.9/7.0
8	0.58	6.7/6.9			
9	1.71	6.9/7.1			

ESP 11		
Layer Number	Layer Thickness, km	V_p, km/s (Top/Bottom)
1	0.09	1.8/3.6
2	0.59	3.6/4.2
3	0.91	4.3/4.3
4	0.78	4.6/4.6
5	0.18	4.5/4.6
6*	0.53	4.6/4.8
7	1.32	5.2/6.1
8	0.87	6.1/6.5
9	1.00	6.5/6.8

V_p, compressional wave velocity; V_s, shear wave velocity.
*Indicates the top of the igneous crust as inferred from comparison of the observed TWTT through the sediments with the TWTT calculated from the velocity depth models given in Table 2.

TABLE 3. Comparison of Velocity-Depth Solutions for ESP and Sonobuoy Profiles

Refraction Line No.	Average V_p* in Upper 1 km of Layer 2, km/s	Contribution to the Intercept Time for a 6.5-km/s Phase Velocity for the Upper 1 km of Layer 2, s
SB 7	5.5 ± 0.2	0.175
SB 10	5.2 ± 0.2	0.215
SB 9	5.5 ± 0.2	0.188
ESP 1	5.4 ± 0.2	0.202
ESP 6	4.4 ± 0.3	0.304
Group 1 average	5.2 ± 0.2	0.217
SB 6	4.6 ± 0.3	0.301
ESP 7	5.1 ± 0.2	0.262
Group 2 average	4.9 ± 0.2	0.282
SB 4	4.4 ± 0.3	0.331
SB 13	4.2 ± 0.3	0.359
ESP 2	4.6 ± 0.3	0.312
Group 3 average	4.4 ± 0.3	0.334
ESP 3	5.0 ± 0.2	0.260
ESP 8	5.2 ± 0.2	0.216
Group 4 average	5.1 ± 0.2	0.238
ESP 9	5.5 ± 0.2	0.186
ESP 4	5.4 ± 0.2	0.206
ESP 11	5.0 ± 0.2	0.166
Group 5 average	5.3 ± 0.2	0.186

*Uncertainties calculated using (1).

high velocity gradient, ranging from velocities between 4.2 and 4.5 km/s at the top to 5.6 and 5.9 km/s at the base (Figure 11). Layer 2B is characterized by a weaker velocity gradient (on the order of 1 s^{-1}). In layer 2C solutions show a further weakening of the velocity gradient to 0.3 s^{-1} necessary to explain the amplitude decay of the arrivals beyond 18 km range. In Figure 11 the differences between the velocity-depth solutions for profiles in this group are not considered to be significant.

The shear wave velocity-depth solutions for group 1 profiles broadly mimic those for the compressional waves (Figure 11). In particular, these solutions require a relatively high shear wave velocity at the top of layer 2A (2.2–2.3 km/s) and a high-velocity gradient. On ESP 1 an increased velocity gradient near the base of layer 2C is necessary to explain the energy triplication peak at 12.5 km range. Near the top of layer 3 the shear wave velocity gradient is reduced (to 0.4 s^{-1} or less) to explain the decay in arrival amplitudes beyond 18 km.

The compressional and shear wave solutions for ESP 1 are compatible with a Poisson's ratio between 0.28 and 0.26 in the upper 1 km of the igneous crust and between 0.24 and 0.28 below this depth (Table 2, Figure 10). The Poisson ratio inferred from the sonobuoy profiles in group 1 also shows this trend towards lower Poisson's ratios (0.35–0.28) with increasing depth. These values are typical of the oceanic crust at these levels [*Hyndman*, 1979; *Spudich and Orcutt*, 1980; *NAT Study Group*, 1985].

Group 2

The average velocity structure inferred for layers 2A and 2B for the group 2 profiles (4.9 ± 0.2 km/s) is marginally lower than that for the group 1 profiles (5.2 ± 0.2 km/s); it accounts for an increased intercept time delay of about 65 milliseconds for the 6.5 km/s refractions (Table 3). The base of layer 2B is characterized by a thin transition zone to typical layer 2C velocities and is necessary to explain the focusing of energy at ranges between 9 and 15 km. The weakening of the velocity gradient in layer 2C is used to explain the rapid decay of amplitudes beyond a distance of 10 km range.

The shear wave solution for ESP 7 also reflects the characteristics of the compressional wave solution for this group (Figure 11). It is typified by a low-velocity gradient at the top of layer 2.

The compressional and shear wave solutions for ESP 7 are consistent with a Poisson's ratio which decreases throughout layer 2 (Figure 11). At the top of layer 2A the Poisson's ratio is inferred to be 0.34; a value typical of porous basalts at DSDP site 504B [*Newmark et al.*, 1985], whereas in layers 2C and 3 Poisson's ratio varies between 0.26 and 0.28. These Poisson's ratios for layers 2C and 3 are typical values for these crustal levels [*Spudich and Orcutt*, 1980; *NAT Study Group*, 1985].

Group 3

The average compressional-wave velocity for layer 2A and 2B (4.4 ± 0.3 km/s) is significantly lower for group 3 than those for group 1 (Table 3). The layer 2A and 2B structure also introduces a significant (nearly 120 ms) additional time delay to the 6.5 km/s arrivals than is introduced by these layers in the group 1 profiles (Table 3). This delay demonstrates that it is not possible to fit the observed travel times for group 3 profiles using the sediment cover used to model group 3 profiles and the layer 2 velocity structure used to model group 1 profiles.

Although the shear wave solution for ESP 2 also has lower velocities in layers 2A and 2B than those for group 1 (Figure 11), these solutions are not well-constrained. The compressional and shear wave solutions for ESP 2 are consistent with a Poisson's ratio between 0.25 and 0.30 for all of layer 2 (Table 2, Figure 11). The Poisson's ratio decreases, although not systematically, with depth.

Group 4

The average velocities in layers 2A and 2B for this group may differ slightly from those of group 1, but they are significantly higher than those for group 3 profiles (Table 3).

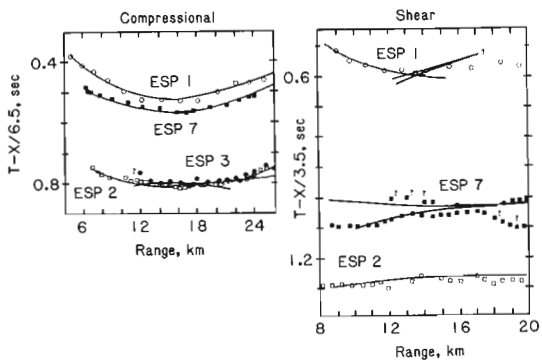

Fig. 9. Expanded comparison of the compressional (left) and shear wave (right) first arrival times for 4 ESP profiles. Solid curves show reduced travel times calculated from the velocity depth models given in Table 2. Travel times only have been corrected to a common datum below sea level of 4370 m. Note the difference in range scales of the figures for the shear and compressional wave travel times. No shear waves were observed on ESP 3.

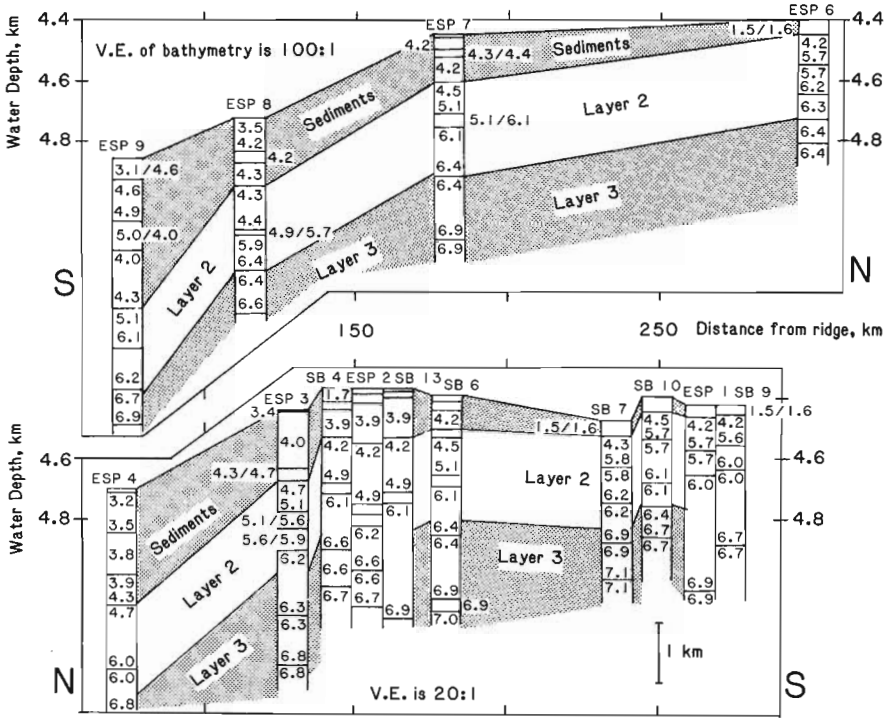

Fig. 10. Comparison of the velocity-depth solutions from north and south of the Hawaiian ridge. Solutions are plotted starting at the top of the sediments through the base of Layer 2. Although no attempt has been made to accurately portray the bathymetry between velocity-depth solutions each solution is plotted starting at the water depth appropriate for the profile. Note difference between bathymetry and crustal structure scaling.

Group 5

The average velocity within layers 2A and 2B for the group 5 profiles is essentially identical to that of group 1 (Table 3). The average calculated delay times through layers 2A and 2B for arrivals having a phase velocity of 6.5 km/s are comparable to those for the group 1 profiles and are 150 ms lower than those for the group 3 profiles (Table 3).

WKBJ Synthetics

WKBJ synthetic seismograms [*Chapman*, 1978; *Chapman and Orcutt*, 1985] calculated from the velocity-depth models in Figure 11 successfully replicate the first-order features observed in the refraction profiles. Figure 12 compares the WKBJ synthetic seismograms calculated for ESPs 1, 2, and 4, which are taken as type examples for groups 1, 3, and 5, respectively. Beyond ranges of 7.5 km the synthetics for ESP 1 show a relatively uniform amplitude distribution with range for the 6.3 to 6.5 km/s refractor out to a range of 18 km and a lack of energy for arrivals having phase velocities significantly less than 6.0 km/s. The synthetics for ESP 2, to the contrary, show the well-developed 4.2 km/s upper crustal refraction and amplitude peak at 9 to 12 km range typical of the group 3 profiles. Beyond 12 km range the amplitude of this phase rapidly decays. The WKBJ synthetics for ESP 4 match the location of the well-developed triplication between 10 and 12 km range, the rapid decay of the 4.2 km/s refractor, and the weak amplitudes of the refractions beyond 13 km range. These synthetics provide additional support for the accuracy of the inferred velocity-depth solutions.

Symmetry of Solutions About the Hawaiian Ridge

The observation that systematic variations in the layer 2 velocity-depth solutions are nearly symmetrically located north and south of Oahu (Tables 1 and 2, Figure 10) is a compelling argument against the explanation of the group 2 and 3 profiles as a localized anomaly.

Previous refraction studies near Oahu also provide evidence for the symmetry of layer 2 about Oahu. Several refraction profiles were collected in the early 1960s in support of Project Mohole [*Shor and Pollard*, 1964; *Morris et al.*, 1969]. These earlier studies, located on Figure 2, between ESPs 6 and 7, generally provided weak constraints on layer 2 velocities because of their coarse (1–1.5 km) shot spacing and the interpretation of travel times only in terms of dipping but homogeneous layers. In agreement with Figure 10, however, *Shor and Pollard* [1964] presented a two-dimensional model which shows a thickening of layer 2 from the arch toward the moat.

Although sediments shed from the Hawaiian ridge are nearly symmetrically distributed north and south of Oahu (Figure 10), it is unlikely that the lower average layer 2 velocities at groups 2 through 4 simply represent misidentified sediments (Table 1). Table 1 documents the fit between the observed TWTT through the sediments and those calculated from the models given in Table 2. Furthermore, the high velocities observed at group 5 profiles can not be explained by misidentified sediments.

Another means of producing the anomalously low-velocity layer 2 in the location of the groups 2 through 4 profiles is the accumulation of a thick sequence of extrusive lava flows on top of the preexisting oceanic crust during the initial stages of the formation of the Hawaiian ridge. *Shor and Pollard* [1964] and *Normark and Shor* [1968] argue that a series of volcanic flows from the ridge may overlie sediments several hundred meters thick. This volcanic layer does not reproduce the observed symmetry of the lowering of the velocities of layers 2A and 2B about the ridge, since a region of lowered velocities is

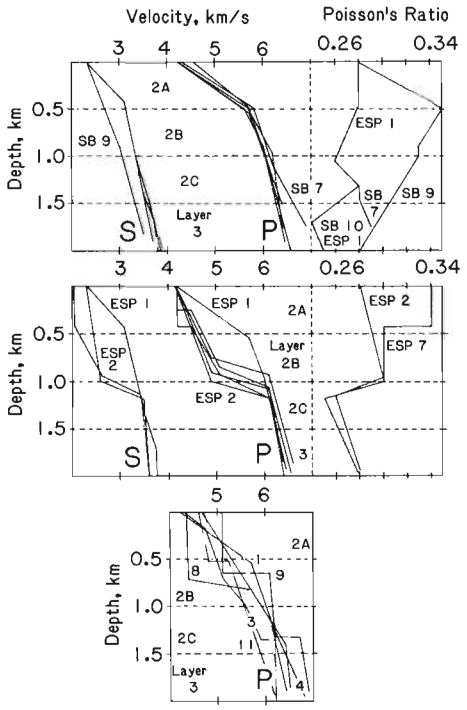

Fig. 11. Compressional and shear velocity-depth solutions and Poisson's ratio inferred from analysis of the travel times. Solutions for group 1 profiles are shown on top, for groups 2 and 3 profiles in the middle, and for groups 4 and 5 profiles on the lowermost part of the figure. Depths plotted are from the top of the igneous crust. Also indicated are the approximate depths of the subdivisions of layer 2. Compressional and shear wave solutions for ESP 1 are repeated for purposes of comparison.

absent at the group 5 profiles. Large seismic reflections from the low-velocity sediments beneath this volcanic layer are not observed in the CDP data (Figures 3, 6, and 7). Thicker crustal sections at the locations of group 2 and 3 profiles than at the group 1 profiles are also not observed [*Watts et al.*, 1985; tBB, 1987].

The observed symmetry in the upper crustal structure about Oahu is even more striking when it is considered that a systematic crustal thickness difference exists north and south of Oahu [*Watts et al.*, 1985; tBB, 1987]. The crust north of Oahu is 0.5–1.0 km thinner than to the south of Oahu. This systematic variation in total crustal thickness is most easily related to the formation of the crust north and south of Oahu at different segments of the spreading center separated by the Molokai fracture zone. The spatial variation observed in the lower crust is thus independent of the variability observed in the upper crust.

Calculations of Strain Associated With Lithospheric Flexure

The symmetry of velocity-depth solutions north and south of Oahu suggests a flexural origin for the lowered velocities in layer 2 at groups 2–4. To compare the geographical location of the velocities with the flexurally induced stresses and strain, calculated stress and strain profiles are shown in Figure 13 for three two-dimensional flexural models of Hawaii calculated assuming thin elastic or elastic-plastic continuous plates, small deflections, planar strains, and a line load. For simplicity of calculation and lack of contrary data, zero deviatoric stresses are assumed in the lithosphere prior to loading. Whereas in the simple elastic plate model no failure is predicted within the plate, a more realistic rheology of the oceanic lithosphere is incorporated into the two elastic-plastic models. For the simple elastic model an elastic plate thickness (T_e) of 25 km was assumed. For the two elastic-plastic models the strength of the oceanic lithosphere is limited by a yield stress envelope (YSE) which describes the stresses at which mechanical failure of the rock occurs and is composed of brittle failure in the form of Byerlee's law in the upper lithosphere and by a temperature-dependent ductile flow in the lower lithosphere [*Goetze and Evans*, 1979].

The strain profiles shown in Figure 13 were derived from the flexural calculations by the following expression:

$$Exx = -Y_n(d^2w/dx^2)$$

where (d^2w/dx^2) is the curvature of the plate, and Y_n is the distance between the neutral surface and the top of the elastic plate [*Hetenyi*, 1974]. The depth to the neutral surface Y_n is constant in the simple elastic plate model but varies with distance from the load in the elastic-plastic models. Stress is related to strain via Young's modulus and Poisson's ratio assuming planar strain. The stress in the elastic-plastic models, however, cannot exceed the YSE, is maximum at the brittle-elastic boundary, and decreases to zero at the surface. The maximum sustained stress, albeit at different depths, is given in the stress profiles (Figure 13).

The flexure calculation used for strain is similar to that given in the work by *Watts et al.* (1985, Figure 5*c*) for the simple elastic model and *ten Brink and Watts* (1985, Figures 2*b* and 2*d*) for the elastic-plastic models. We use the 44-m.y.-

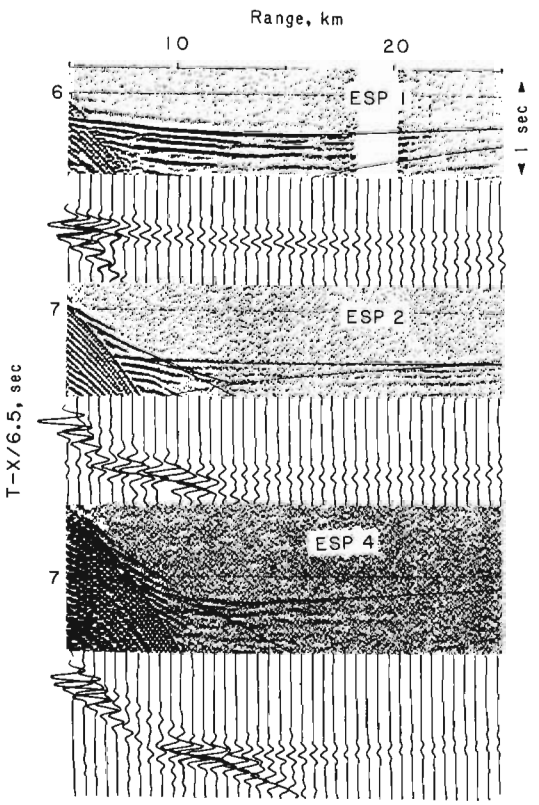

Fig. 12. Comparison of ESP profiles and WKBJ synthetic seismograms calculated for the compressional wave arrivals for ESPs 1 (top), 2 (middle), and 4 (bottom), which are considered to be type examples for groups 1, 3, and 5. Both observed and synthetic profiles are reduced at 6.5 km/s and are plotted in true relative amplitude.

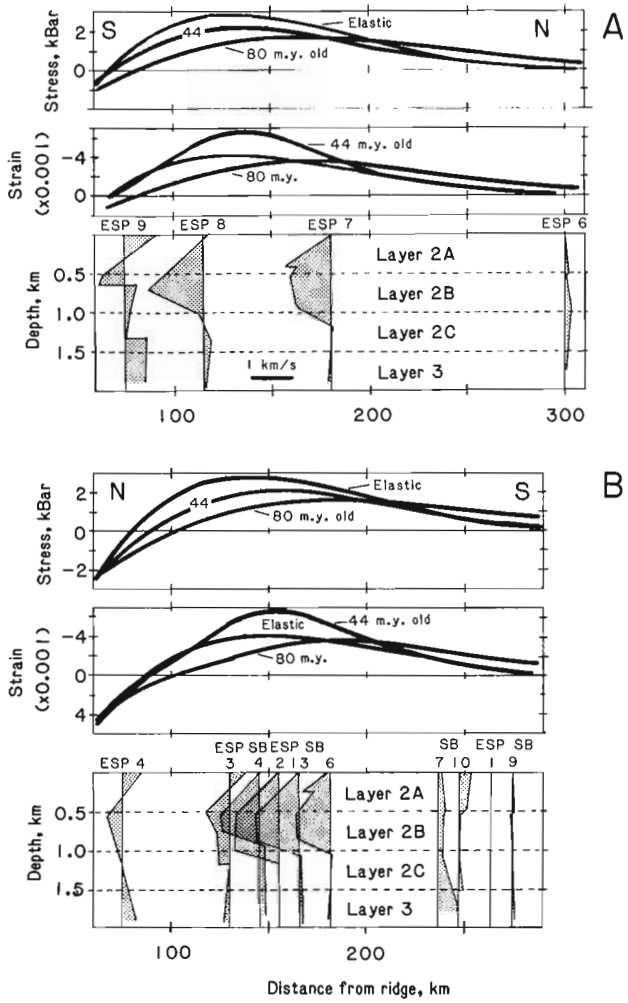

Fig. 13. (*a*) Comparison of the elastic stresses at the brittle-elastic boundary and strains in the upper crust calculated for a simple elastic lithosphere (T_e = 25 km) as well as for two elastic-plastic lithospheres having yield stress envelopes appropriate for 44 and 80 m.y. ages and loaded by the Hawaiian ridge. In this figure positive stresses and negative strains are extensional. The geometry of the load assumed is that used by *ten Brink and Watts* [1985]. Also shown as a function of distance from the center of the load (the Hawaiian ridge) are the compressional wave velocity anomalies relative to ESP 1 of group 1. Velocity anomalies are plotted starting at the top of Layer 2. (*b*) Same as Figure 13*a* but for study area south of Oahu.

old lithosphere model in Figure 13 based on the conclusion reached by *ten Brink and Watts* [1985] that a more accurate fit to the observed stratigraphy in the sedimentary moat surrounding Oahu is achieved by assuming a lithosphere having a thermal age of 44 m.y. rather than the 80-m.y. seafloor age near Hawaii.

Figure 13 also compares velocity anomalies, calculated by subtracting the compressional wave solution for ESP 1 of group 1 from each compressional wave velocity solution, to the calculated stresses and strains. The group 1 profiles have almost no velocity anomaly and are located at ranges corresponding to the nearly unflexed portion of the lithosphere where the calculated tensional strains are less than 6.8×10^{-4} and calculated tensional stresses at the brittle-elastic boundary are below 1.2 kbar (1 kbar = 10^8 Pa). The group 2–4 refraction profiles showing significant negative velocity anomalies in layers 2A and 2B are located at ranges corresponding to the maximum calculated extensional strains associated with the lithospheric flexure. The calculated tensional stresses and extensional strains predicted by the simple elastic theory are nearly 30 times larger in this region than outside of the arch. The normal to slightly high-velocity group 5 profiles are located where the lithosphere is predicted to be in compression for all three flexural models, although these higher velocities may also be partly caused by the increased sediment load in this distance range. Differences in the locations of the maximum strain peaks predicted by these models to the north and south of Oahu are consistent with the asymmetry of the load; previous two-dimensional gravity calculations suggest that the northern half of the Hawaiian ridge is best modeled as being less massive than the southern half [*Watts et al.*, 1985].

In Figure 14 we plot the average layer 2 velocity for each ESP with the predicted tensional strain for the location of each ESP calculated for the 44-m.y.-old lithosphere. The average layer 2 velocity for each ESP was calculated from the vertical two-way travel time through the uppermost 1.0 km of layer 2 shown in Figure 11 and are provided in Table 3. The uncertainties in seismic velocities shown in Table 3 and Figure 14 were calculated using (1) and the discussion following (1). These averages document a simple inverse relationship between the theoretical strain and the compressional and shear wave velocities, suggesting that as the predicted extensional strain increases, average velocities decrease. Excluding ESP 6, which is clearly anomalous within group 1, the correlation coefficient of the average compressional-wave solutions and strains for the 44-m.y.-old lithosphere is 0.818.

Discussion

Figures 13 and 14 document the inverse correlation between average velocities in layer 2 and the calculated stresses and strains caused by the lithospheric flexuring. This correlation is not strongly dependent on any particular flexural model but

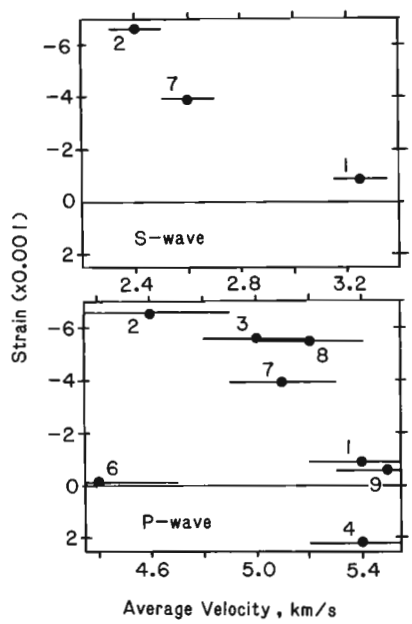

Fig. 14. Comparison of the theoretical strains calculated for the flexure of 44 m.y. old lithosphere with the average compressional wave velocities in the upper 1.0 km of the igneous crust. As is described in the text, the average velocity is calculated from the vertical two-way travel time through the upper 1 km of the igneous crust. Error bars on average velocities are calculated from (1). Negative strains are extensional.

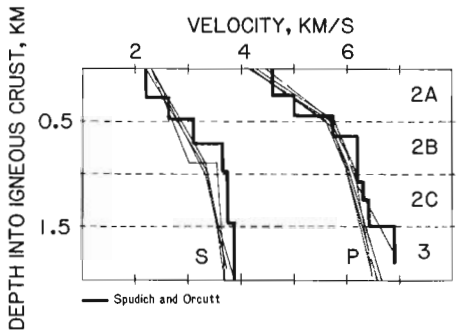

Fig. 15. Comparison of the compressional and shear wave velocity-depth solutions for the group 1 profiles (light solid curves) with the published results of *Spudich and Orcutt* [1980] from the Fanfare site in the East Pacific (bold solid curves). Approximate depths of the subdivisions of layer 2 are also indicated.

appears to be most consistent with the model of a 44-m.y.-old lithosphere. An independent test of the dependence of layer 2 velocities with lithospheric flexure involves a comparison of the solutions from near Oahu to other high-quality refraction measurements from the Pacific Ocean to determine whether the group 1 profiles are representative of unflexed oceanic crust.

Velocity-depth solutions from outside the Hawaiian arch resemble those from the well-studied Fanfare data from 15 m.y. old crust off Guadalupe Island in the East Pacific [*Spudich and Orcutt*, 1980]. The Fanfare experiment was located within 110 km of Guadalupe Island. Because the compensation near Guadalupe Island is more localized than at Hawaii since Guadalupe was formed on the ridge or on very young seafloor, however, the crust at the Fanfare site does not show anomalously low velocities in layer 2. The agreement between the compressional and shear velocity depth solutions for group 1 profiles and the Fanfare solutions is close (Figure 15) and rather surprising considering that these two areas have significantly different crustal ages and that the interpretational styles of the two refraction datasets differ.

The agreement between the Hawaii and Fanfare velocity-depth solutions is important because *Spudich and Orcutt* [1980] have carefully studied the consequences of their models in terms of the petrology and porosity of the igneous crust. In particular, they explained the strong velocity gradient in layer 2A at the Fanfare site by a drop in porosity from an estimated 18% to approximately 2%. This porosity drop matches that inferred from electrical resistivity measurements in layer 2 at DSDP site 504B in the East Panama Basin [*Anderson et al.*, 1982; *Becker et al.*, 1982; *Bratt and Purdy*, 1984]. One possibility then, is that the similarity between the Hawaiian solutions for group 1 profiles and the Fanfare results suggests that the porosity-depth structures are similar at the Fanfare and group 1 sites. Results from DSDP site 504B suggest that the lowered layer 2A and 2B velocities inside of the Hawaiian arch at ranges close to 160 km may be explained by basalts having higher porosities relative to "normal" oceanic crust at the same depth. It is important to note, however, that many other factors, most of them difficult to estimate, exert strong influences on the elastic velocities in a saturated cracked solid [*Purdy and Ewing*, 1986]. For instance, *Spudich and Orcutt* [1980] pointed out that the elastic velocities of a saturated, cracked solid may be extremely sensitive to the differential pressure within the cracks.

Our preferred model for seismic layer 2 suggests a primary dependence of the velocities on porosity and the effective confining pressure, which is based on laboratory measurements of basalts. The group 2 and 3 profiles have average velocity anomalies of -0.4 to -0.5 ± 0.2 km/s in layers 2A and 2B (Figure 13) at locations where the tensional stresses predicted by the flexural models are the highest. To determine whether the magnitudes of the velocity anomalies are consistent with reasonable estimates of stress drops produced by these increased tensional stresses, minimum stress drops were calculated from Byerlee's law assuming no further stress reduction by crack opening. In this case Byerlee's law states that the shear stress τ necessary to overcome static friction on a surface having a normal stress, σ_n, across it is $\tau = 0.85\sigma_n$ for $\sigma_n < 2$ kBar [*Kirby*, 1983]. For groups 2–4 the predicted elastic-brittle boundary lies below layer 2 and thus the rocks in layer 2 will fail in tension according to Byerlee's law. Recasting this relationship in terms of principal stresses for faults favorably oriented to support a minimum stress difference one obtains for σ_h less than 1.2 kbar:

$$\sigma_{zz} - \sigma_h = 0.8\sigma_{zz}$$

in tension, where σ_{zz} is the vertical stress, and σ_h is the horizontal stress [*Kirby*, 1980]. Thus as long as the stress reduction behaves plastically, the maximum horizontal stress drop at the top 1 km of the igneous crust will be about 0.8 kbar (from 1 to 0.2 kbar). Although these estimated deviatoric stress drops are not strictly comparable to hydrostatic stress drops, laboratory measurements document that at confining pressures of 1 kbar a drop to 0.2 kbar confining pressure is sufficient to decrease compressional wave velocities by 0.5 km/s in the high-porosity basalts expected to comprise layers 2A and 2B [*Manghnani and Woollard*, 1968]. Low confining pressures between 0.4 and 1.1 kbar are predicted for the top of layer 2 by simple lithostatic calculations for all the groups, so a deviatoric stress drop of 0.8 kbar should significantly affect the elastic wave velocities of the basalts in layer 2 near Oahu. Only at the locations of groups 2–4 are the magnitudes of the predicted tensional stresses sufficient to significantly reduce the average elastic velocities.

Laboratory measurements also provide an explanation for the absence of a detectable velocity anomaly in layers 2C and 3 (Figure 13). Rocks in these layers are currently presumed to represent rocks transitional to the sheeted dikes and the dikes themselves, respectively, and thus have lower porosities than the overlying basalts [*Anderson et al.*, 1982; *Bratt and Purdy*, 1984]. *Manghnani and Woollard* [1968] show that basalts having low (<3%) porosity display a significantly lower velocity dependence on confining pressure (<0.25 km/s) than do high-porosity (>10%) basalts. Furthermore, the laboratory results reported by Manghnani and Woollard for Hawaiian basalts indicate that the percentage velocity decrease diminishes with increasing confining pressure which would occur as one moves lower into layers 2 and 3.

Of considerable interest is whether the high extensional strains near the group 2 and 3 profiles caused by the lithospheric flexure lead to anelastic deformation of the crust. Although laboratory measurements show little velocity hysteresis [*Manghnani and Woollard*, 1968] and are thus compatible with an elastic opening of preexisting cracks, they are based on centimeter sized samples and ignore the large-scale fractures which refraction techniques sample. Nor do these laboratory measurements simulate the long-term effect of lower stress in layer 2 and the possible in-filling of the opened cracks by low-temperature precipitates. Most importantly, however,

it seems unlikely that the large tensional stresses predicted by the flexural models can be maintained in the higher crustal levels where they exceed the confining pressures. It seems more likely that in the upper crust where confining pressures are exceeded by flexurally induced stresses these tensional stresses were accomodated by failure.

Evidence for anelastic deformation of the lithosphere during the flexure includes normal faulting observed on CDP records in the upper crust within the arch on ESP 3 (Figure 7) and offsets in the inferred Moho reflection below (tBB, 1987). These observations are in agreement with the depth of brittle failure predicted by these flexural models.

The locations of low velocities in layer 2 within the Hawaiian arch correlate with the locations of predicted strains calculated to be on the order of 0.5%. A similar elastic-plastic plate model predicts strains on the order of 5% seaward of some trench systems which produced observable velocity anomalies determined from sonobuoy measurements near the Izu-Bonin trench [*Bodine et al.*, 1981]. That evidence for lowered layer 2 velocities is observable over nearly 2 orders of magnitude in predicted extensional strains suggests that upper crustal velocities may be used to constrain flexural models in other trenches where lesser strains are expected than at the Izu-Bonin trench. Although the Hawaiian ridge represents one of the largest midplate loads superimposed upon oceanic lithosphere, strains in the upper crust comparable to those predicted near the Hawaiian ridge are expected near other large midplate volcanic chains, oceanic plateaus, and possibly near passive margins. Figure 13 illustrates that these strains will be amplified when there has been a significant thermal perturbation to the underlying lithosphere.

Summary and Conclusions

Detailed travel time and amplitude modeling of 15 high-quality digitally recorded refraction profiles on the flexed Pacific lithosphere surrounding the Hawaiian ridge reveals a significant, systematic, and symmetric dependence of average layer 2 velocities on their position relative to the Hawaiian ridge. These velocity differences are typified by three distinct groups (groups 1, 2–4, and 5) of closely spaced refraction profiles, each consisting of three or more measurements. Comparison of the velocity-depth solutions inferred from these refraction profiles with the extensional and compressional strains predicted for an elastic-plastic plate flexed by the load of the Hawaiian ridge (Figure 14) shows a significant inverse relationship over the range of strains examined for the model of the 44-m.y.-old oceanic lithosphere. We suggest that the lowered velocities in layer 2 near the Hawaiian arch are related to the increased extensional strains and crack opening due to the lithospheric flexure.

The results obtained in this experiment demonstrate that determination of the three-dimensional distribution of average layer 2 velocities may provide additional constraints on the stresses and strains predicted for models for the flexure of the oceanic lithosphere. These constraints could be made even more powerful if a more rigorous determination of the increased stress or strain could be inferred from these velocity measurements. This type of seismic approach to the study of lithospheric flexure is attractive because, as we have argued in this paper, a large number of closely spaced high-quality sonobuoy refraction profiles obtained from a single ship towing a large airgun array provide an adequate dataset for this type of investigation. Densely spaced sonobuoy profiles may thus be an indirect means of evaluating the relative flexural stresses and strains of the lithosphere at subducting trenches, mid-ocean spreading centers, passive margins, and large midplate loads.

We emphasize, however, that deviatoric stresses imposed by lithospheric flexure are the inferred origin of the observed velocity anomalies near Oahu. Thus other oceanic regions having anomalous stress regimes for any reason, including lithospheric flexure, may also be places of anomalous layer 2 structure. Examples of such regions are those portions of the Indian-Australian plate having large-amplitude bathymetric folds and geoidal rolls of approximately 200 km wavelength [*Weissel et al.*, 1980; *McAdoo and Sandwell*, 1985]. In these regions large (>2 kbar) compressive stresses are predicted based on finite element calculations of the Indian plate [*Cloetingh and Wortel*, 1985] as well as by calculations of the stresses necessary to produce folds in an elastic-plastic lithosphere to the observed amplitudes [*McAdoo and Sandwell*, 1985]. Such regions in the Indian Ocean are predicted by the proposed model to have anomalously high velocities in layer 2.

It appears likely that given the similarities in the seismic signature produced by the flexuring to previously published refraction results in the Pacific Ocean, the effects of lithospheric flexure on the upper crustal structure are widespread throughout the oceans. It may be fruitful, therefore to reassess previous refraction results for layer 2 bearing the state of upper lithospheric stress of each site in mind.

Acknowledgments. We thank P. Buhl and J. Alsop and the rest of the Multichannel Seismic group at Lamont-Doherty Geological Observatory for their assistance in the processing of the ESP and CDP data, D. Lindwall for reducing the sonobuoy refraction data, D. Dubois and C. Ebinger for their help in digitizing travel times, and G. M. Purdy for his explanation of the WKBJ and the ray tracing programs used to generate theoretical travel times and seismograms. We thank T. Duennebier and B. Wedgewood for helping to compile the detailed bathymetric maps. We thank P. Buhl and E. Vera for many helpful discussions. We thank E. Ambos, J. Collins, D. Hill, J. Karson, J. Mutter, and A. B. Watts for careful reviews of earlier drafts of this manuscript. This work was supported by NSF grants OCE81-171210 (Hawaii Institute of Geophysics) and OCE84-43349 (WHOI) and OCE81-11704 (LDGO). Woods Hole Oceanographic Institution Contribution 6132. Lamont-Doherty Geological Observatory Contribution 4024.

References

Anderson, R. N., et al., DSDP hole 504B, the first reference section over 1 km through layer 2 of the oceanic crust, *Nature*, *300*, 589–594, 1982.

Atwater, T., and H. W. Menard, Magnetic lineations in the northeast Pacific, *Earth Planet. Sci. Lett.*, *7*, 445–450, 1970.

Becker, K., et al., In-situ electric resistivity and bulk porosity of the oceanic crust, Costa Rica Rift, *Nature*, *300*, 594–598, 1982.

Bodine, J. H., M. S. Steckler, and A. B. Watts, Observations of flexure and the rheology of the oceanic lithosphere, *J. Geophys. Res.*, *86*, 3695–3707, 1981.

Brace, W. F., and D. L. Kohlstedt, Limits on lithospheric stress imposed by laboratory experiments, *J. Geophys. Res.*, *85*, 6248–6252, 1980.

Bratt, S. R., and G. M. Purdy, Structure and variability of oceanic crust on the flanks of the east Pacific Rise between 11° and 13°N, *J. Geophys. Res.*, *89*, 6111–6125, 1984.

Cann, J. R., A model for oceanic crustal structure developed, *Geophys. J.R. Astron. Soc.*, *39*, 169–187, 1974.

Chapman, C. H., A new method for computing synthetic seismograms, *Geophys. J.R. Astron. Soc.*, *54*, 481–518, 1978.

Chapman, C. H., and J. A. Orcutt, The computation of body-wave synthetic seismograms, *Rev. Geophys. Space Phys.*, *23*, 105–163, 1985.

Christensen, N. I., Ophiolites, seismic velocities and oceanic crustal structure, *Tectonophysics*, *47*, 131–157, 1978.

Cloetingh, S., and R. Wortel, Regional stress field of the Indian Plate, *Geophys. Res. Lett.*, *12*, 77–80, 1985.

Diebold, J. B., and P. L. Stoffa, The travel-time equation, tau-p mapping and inversion of common midpoint data, *Geophysics*, *46*, 238–254, 1981.

Fox, P. J., and J. B. Stroup, The plutonic foundation of the oceanic crust, in *The Sea*, vol. 7, edited by C. Emiliani, pp. 119–218, John Wiley, New York, 1981.

Goetze, C., and B. Evans, Stress and temperature in the bending lithosphere as constrained by experimental rock mechanics, *Geophys. J. R. Astron. Soc.*, *59*, 463–478, 1979.

Hetenyi, M., *Beams on Elastic Foundations*, 255 pp., University of Michigan Press, Ann Arbor, 1974.

Houtz, R. E., and J. Ewing, Upper crustal structure as a function of plate age, *J. Geophys. Res.*, *81*, 2490–2498, 1976.

Houtz, R. E., C. Windisch, and S. Murauchi, Changes in the crust and upper mantle near the Japan-Bonin Trench, *J. Geophys. Res.*, *85*, 267–274, 1980.

Hussong, D. M., M. E. Odegard, and L. K. Wipperman, Compressional faulting of the oceanic crust prior to the subduction in the Peru-Chile trench, *Geology*, *3*, 601–604, 1975.

Hyndman, R. D., Poisson's ratio in the oceanic crust—A review, *Tectonophysics*, *59*, 321–333, 1979.

Kirby, S. H., Tectonic stresses in the lithosphere: Constraints provided by experimental deformation of rocks, *J. Geophys. Res.*, *85*, 6353–6363, 1980.

Kirby, S. H., Rheology of the lithosphere, *Rev. Geophys. Space Phys.*, *21*, 1458–1487, 1983.

Kroenke, L. W., Seismic reflection studies of sediment thickness around the Hawaiian ridge, *Pac. Sci.*, *19*, 335–338, 1965.

Manghnani, M. H., and G. P. Woollard, Elastic wave velocities in Hawaiian rocks at pressures to ten kilobars, in *The Crust and Upper Mantle of the Pacific Area*, edited by L. Knopoff, C. L. Drake, and P. J. Hart, pp. 501–516, AGU, Washington, D.C., 1968.

McAdoo, D. C., and D. T. Sandwell, Folding of oceanic lithosphere, *J. Geophys. Res.*, *90*, 8563–8569, 1985.

Morris, G. B., R. W. Raitt, and G. G. Shor, Velocity anisotropy and delay time maps of the mantle near Hawaii, *J. Geophys. Res.*, *74*, 4300–4316, 1969.

NAT Study Group, North Atlantic Transect (NAT): A wide-aperture, two-ship multichannel seismic investigation of the oceanic crust, *J. Geophys. Res.*, *90*, 10,321–10,341, 1985.

Ness, G., S. Levi, and R. Couch, Marine magnetic anomaly timescales for the Cenozoic and the late Cretaceous: A precis, critique, and synthesis, *Rev. Geophys. Space Phys.*, *18*, 753–770, 1980.

Newmark, R. L., R. N. Anderson, D. Moos, and M. D. Zoback, Structure, porosity and stress regime of the upper oceanic crust: Sonic and ultrasonic logging of DSDP Hole, 504B, *Tectonophysics*, *118*, 1–42, 1985.

Normark, W. R., and G. G. Shor, Jr., Seismic reflection study of the shallow structure of the Hawaiian Arch, *J. Geophys. Res.*, *73*, 6991–6998, 1968.

Purdy, G. M., and J. I. Ewing, Seismic structure of the ocean crust, in *The Geology of North America: The Western Atlantic Region*, vol. 1, edited by B. E. Tucholke and P. R. Vogt, Geological Society of America, Boulder, Colo., 1986.

Shor, G. G., and D. D. Pollard, Mohole site selection studies north of Maui, *J. Geophys. Res.*, *69*, 1627–1637, 1964.

Spudich, P., and J. Orcutt, Petrology and porosity of an oceanic crustal site: Results from wave form modelling of seismic refraction data, *J. Geophys. Res.*, *85*, 1409–1433, 1980.

Ten Brink, U. S., and A. B. Watts, Seismic stratigraphy of the flexural moat flanking the Hawaiian Islands, *Nature*, *317*, 421–424, 1985.

Von Herzen, R. P., R. S. Detrick, S. T. Crough, D. Epp, and U. Fehn, Thermal origin of the Hawaiian swell: Heat flow evidence and thermal models, *J. Geophys. Res.*, *87*, 6711–6724, 1982.

Walcott, R. I., Flexure of the lithosphere at Hawaii, *Tectonophysics*, *9*, 435–446, 1970.

Wallin, B. H., The northern Hawaiian deep and arch: Interpretation of geologic history from reflection profiling and echo character mapping, M.S. thesis, Univ. of Hawaii, Honolulu, 1982.

Watts, A. B., and J. R. Cochran, Gravity anomalies and flexure of the lithosphere along the Hawaiian-Emperor seamount chain, *Geophys. J.R. Astron. Soc.*, *38*, 119–141, 1974.

Watts, A. B., U. S. ten Brink, P. Buhl, and T. M. Brocher, A multichannel seismic study of lithospheric flexure across the Hawaiian-Emperor seamount chain, *Nature*, *315*, 105–111, 1985.

Weissel, J. K., R. N. Anderson, and C. A. Geller, Deformation of the Indo-Australian plate, *Nature*, *287*, 284–291, 1980.

White, R. S., and R. A. Stephen, Compressional to shear wave conversion in oceanic crust, *Geophys. J.R. Astron. Soc.*, *63*, 547–565, 1980.

Whitmarsh, R. B., Seismic refraction studies of the upper igneous crust in the north Atlantic and porosity estimates for layer 2, *Earth Planet Sci. Lett.*, *37*, 431–464, 1978.

Winterer, E. L., et al., *Initial Reports of the Deep Sea Drilling Project*, vol. 7, U. S. Government Printing Office, Washington, D. C., 1971.

T. M. Brocher, U.S. Geological Survey, 345 Middlefield Road, MS 977, Menlo Park, CA 94025.

U. S. ten Brink, Lamont-Doherty Geological Observatory and the Department of Geological Sciences of Columbia University, Palisades, NY 10964.

(Received February 25, 1986;
revised November 20, 1986;
accepted November 21, 1986.)